JOURNAL OF PROPULSION AND POWER
Vol. 26, No. 5, September–October 2010

Numerically Simulated Comparative Performance of a Scramjet and Shcramjet at Mach 11

Jonathan Chan* and Jean P. Sislian†
University of Toronto, Toronto, Ontario M3H 5T6, Canada
and
Derrick Alexander‡
Martec, Ltd., Halifax, Nova Scotia B3J 3J8, Canada

DOI: 10.2514/1.48144

The aeropropulsive performance characteristics of a scramjet and a shock-induced combustion ramjet (shcramjet) are compared at a flight Mach number of 11 and an altitude of 34.5 km. The vehicles share the same inlet type, fuel injection system, fuel/air equivalence ratio, mixing/combustor duct, methodology of nozzle design, and gridding technique. The numerical simulation of the three-dimensional vehicle flowfields from tip to tail are performed by the window allocatable resolver for propulsion code, in which the multispecies Favre-averaged Navier–Stokes equations are closed by the Wilcox k-ω turbulence model. Combustion is simulated by the H_2-air chemical kinetics model of Jachimowski. Magnitudes of the thrust, fuel-specific impulse, pressure, and frictional forces acting on the vehicles are determined. Results show that the scramjet outperforms the shcramjet with a fuel-specific impulse of 1450 s as opposed to 1109 s developed by the shcramjet. However, the shcramjet is appreciably smaller and thus lighter than the scramjet with a combustor length which is one-fifth of the scramjet combustor length, requiring much less cooling.

Nomenclature

c_k	=	mass fraction of species k
c_p	=	specific heat at constant pressure
D_k	=	mass diffusion coefficient of species k
d_w	=	distance from wall to first inner node
E	=	total specific energy, $e + k + 1/2q^2$
e	=	specific internal energy
$\mathcal{F}_{\text{friction}}$	=	frictional force
$\mathcal{F}_{\text{fuel}}$	=	fuel thrust
$\mathbf{F}_i$	=	convection flux vector in the i direction
$\mathcal{F}_{\text{pot}}$	=	thrust potential
$\mathcal{F}_{\text{pressure}}$	=	pressure force
$\mathbf{G}$	=	vector of diffusion variables
h_k	=	enthalpy of species k
I_{sp}	=	specific impulse
J	=	metric Jacobian
$\mathbf{K}_{i,j}$	=	diffusion matrix
k	=	turbulent kinetic energy
M_T	=	turbulent Mach number, $\sqrt{2k}/a$
$\dot{m}$	=	mass flow rate
nd	=	number of dimensions
ns	=	number of species
P_k	=	production of turbulent kinetic energy
Pr_T	=	turbulent Prandtl number
p	=	pressure
$p^\star$	=	effective pressure, $p + 2/3\rho k$
$\mathbf{Q}$	=	conserved variables
q	=	magnitude of velocity vector
$\mathbf{R}$	=	residual
$\mathbf{S}$	=	source terms
Sc_T	=	turbulent Schmidt number
T	=	temperature
V_i	=	contravariant velocity
v_i	=	velocity component in the i direction
$\dot{W}_k$	=	chemical production rate of species k
X_i	=	curvilinear coordinate in the i direction
$X_{i,j}$	=	$\partial X_i/\partial x_j$
x_i	=	Cartesian coordinate in the i direction
y^+	=	nondimensional wall distance, $d_w\rho\sqrt{\tau_w/\rho_w}/\mu$
$\beta^{r,s}_{i,j}$	=	$\alpha_{i,j}\delta_{r,s} + J^{-1}X_{i,s}X_{j,r} - 2/3J^{-1}X_{i,r}X_{j,s}$
δ_{ij}	=	Kronecker delta
δ_{X_i}	=	discrete derivative with respect to X_i
η_m	=	mixing efficiency
κ	=	thermal conductivity
μ	=	viscosity
μ_T	=	turbulent eddy viscosity
ξ	=	convergence criterion
ρ	=	density
σ_k	=	Wilcox turbulent closure coefficient
σ_ω	=	Wilcox turbulent closure coefficient
τ	=	pseudotime
τ_w	=	wall shear stress
ω	=	dissipation rate per unit of turbulent kinetic energy

I. Introduction

THE supersonic combustion ramjet (scramjet) has established itself as the engine of choice to propel hypersonic vehicles and has been developed into practical engine hardware for a number of hypersonic experimental vehicles. However, it is widely acknowledged that, as the flight Mach number increases well beyond 10–12, its combustor may become excessively long due to the diffusive burning taking place in very high air velocities in the combustor of the order of 3000–5000 m/s. Excessive weight and cooling requirements may then pose serious technological challenges for its practical implementation. As a possible alternative, it has been suggested to decouple the fuel/air mixing and burning processes.

Presented at the 48th AIAA Aerospace Sciences Meeting, Orlando, FL, 4–7 January 2010; received 20 November 2009; revision received 27 April 2010; accepted for publication 28 April 2010.

*Graduate Student, Institute for Aerospace Studies, High Speed Vehicle Propulsion Systems Group, 4925 Dufferin Street; jonathan_chan@alumni.utoronto.ca.

†Professor, Institute for Aerospace Studies, High Speed Vehicle Propulsion Systems Group, 4925 Dufferin Street; sislian@caius.utias.utoronto.ca. Associate Fellow AIAA.

‡Research Associate, High Speed Vehicle Propulsion Systems Group, 4925 Dufferin Street; currently Research Scientist, Halifax; dalexander@martec.com. Senior Member AIAA.

Fuel is injected well ahead of the combustor in the long forebody/inlet of the vehicle while avoiding its premature ignition, especially in the forebody boundary layer, and the combustible mixture is ignited through an appropriately located shock wave. The ignition and combustion is then rapid, resulting in a very short combustor. This concept of hypersonic propulsion has been variously named the oblique detonation wave engine, wave combustor or shock-induced combustion ramjet (shcramjet), and has been investigated for the last two to three decades by several researchers [1–5].

From this body of research, a consensus has emerged that the shcramjet can outperform the scramjet at flight Mach numbers above 10–12. However such conclusions were based on a number of restrictive assumptions. In [4], performance and sizing estimates were made using an engineering hypersonic vehicle synthesis code with various assumptions, whereas in [5], planar and/or axisymmetric Euler equations of motion were used with a finite-rate H_2/air chemical kinetics model. The fuel-specific impulse of the shcramjet as a function of the flight Mach number was then compared with that of the scramjet given by Heiser and Pratt [6].

The present paper reports results of a three-dimensional numerical simulation of the aeropropulsive performance characteristics of a scramjet and a shcramjet at a flight Mach number of 11. The study is based on multispecies Favre-averaged Navier–Stokes equations closed by a turbulence model and an H_2/air chemical kinetics model. A brief description of the governing equations, the numerical method employed, the boundary conditions imposed on the integration domain and the performance parameters used to estimate aeropropulsive characteristics of both vehicles are given in the next paragraph. A detailed description of these topics together with the validation efforts of the numerical technique against experimental data are presented elsewhere [7–9]. This is followed by a comprehensive description of conditions and assumptions made for engine component modelling, with detailed analysis of their respective flowfields. Comparative aeropropulsive performance characteristics of the entire vehicle from tip to tail are considered next. A final paragraph summarizes the main findings of the performed study.

II. Governing Equations

Investigated flowfields are described by the Favre-averaged Navier–Stokes equations, closed by the k-ω turbulence model of Wilcox [10] and the 9-species, 20-reaction Jachimowski [11] H_2-air chemical kinetics model (nitrogen is assumed to be an inert gas). The equations are expressed in generalized coordinates as $\partial \mathbf{Q}/\partial\tau = -\mathbf{R}$, where minimization of the residual is sought:

$$\mathbf{R} = \sum_{i=1}^{nd}\left[\frac{\partial \mathbf{F}_i}{\partial X_i} - \sum_{j=1}^{nd}\frac{\partial}{\partial X_i}\left(\mathbf{K}_{i,j}\frac{\partial \mathbf{G}}{\partial X_j}\right)\right] - \mathbf{S} \tag{1}$$

For the conservative variable, convective flux, and diffusion term, we have

$$\mathbf{Q} = \frac{1}{J}\begin{bmatrix} \rho c_1 \\ \vdots \\ \rho c_{ns} \\ \rho v_1 \\ \vdots \\ \rho v_{nd} \\ \rho E \\ \rho k \\ \rho \omega \end{bmatrix}, \qquad \mathbf{F}_i = \frac{1}{J}\begin{bmatrix} \rho V_i c_1 \\ \vdots \\ \rho V_i c_{ns} \\ \rho V_i v_1 + X_{i,1} p^\star \\ \vdots \\ \rho V_i v_{nd} + X_{i,nd} p^\star \\ \rho V_i E + V_i p^\star \\ \rho V_i k \\ \rho V_i \omega \end{bmatrix}$$

$$\mathbf{G} = \begin{bmatrix} c_1 \\ \vdots \\ c_{ns} \\ v_1 \\ \vdots \\ v_{nd} \\ T \\ k \\ \omega \end{bmatrix} \tag{2}$$

where

$$V_i = \sum_{m=1}^{nd} X_{i,m} v_m$$

is the contravariant velocity. The total energy and effective pressure include molecular and turbulent components, $E = e + k + 1/2q^2$ and $p^\star = p + 2/3\rho k$. The internal energy, enthalpy, and specific heat at constant pressure are determined from temperature dependent polynomials from McBride and Reno [12], whereas p is found through the ideal gas law from the temperature and density. With

$$\alpha_{i,j} = J^{-1}\sum_{m=1}^{nd} X_{i,m} X_{j,m}$$

the diffusion matrix can be shown to be

$$\mathbf{K}_{i,j} = \begin{bmatrix} \alpha_{i,j} D_1^\star & \cdots & 0 & 0 & \cdots & 0 & 0 & 0 & 0 \\ \vdots & \ddots & \vdots & \vdots & \ddots & \vdots & \vdots & \vdots & \vdots \\ 0 & \cdots & \alpha_{i,j} D_{ns}^\star & 0 & \cdots & 0 & 0 & 0 & 0 \\ 0 & \cdots & 0 & \mu^\star \beta_{i,j}^{1,1} & \cdots & \mu^\star \beta_{i,j}^{1,nd} & 0 & 0 & 0 \\ 0 & \cdots & 0 & \vdots & \ddots & \vdots & 0 & 0 & 0 \\ 0 & \cdots & 0 & \mu^\star \beta_{i,j}^{nd,1} & \cdots & \mu^\star \beta_{i,j}^{nd,nd} & 0 & 0 & 0 \\ \alpha_{i,j} h_1 D_1^\star & \cdots & \alpha_{i,j} h_{ns} D_{ns}^\star & \mu^\star \sum_{k=1}^{ns} v_k \beta_{i,j}^{k,1} & \cdots & \mu^\star \sum_{k=1}^{ns} v_k \beta_{i,j}^{k,nd} & \alpha_{i,j}\kappa^\star & \alpha_{i,j}\mu_k^\star & 0 \\ 0 & \cdots & 0 & 0 & \cdots & 0 & 0 & \alpha_{i,j}\mu_k^\star & 0 \\ 0 & \cdots & 0 & 0 & \cdots & 0 & 0 & 0 & \alpha_{i,j}\mu_\omega^\star \end{bmatrix} \tag{3}$$

For the effective viscosity, thermal conductivity, mass diffusion, and diffusion coefficients of the turbulent kinetic energy and length scale determining equations, we have $\mu^\star = \mu + \mu_T$, $\kappa^\star = \kappa + c_p\mu_T/Pr_T$, $D_k^\star = D_k + \mu_T/Sc_T$, $\mu_k^\star = \mu + \mu_T/\sigma_k$, and $\mu_\omega^\star = \mu + \mu_T/\sigma_\omega$. Based on dimensional analysis arguments, the turbulent viscosity can be written as $\mu_T = 0.09\rho k/\omega$. The turbulent Prandtl number, σ_k, and σ_ω are set to 0.9, 2.0, and 2.0, respectively, while the turbulent Schmidt number is set to 1.0 and not altered in space. The source term includes the chemical species production terms and the baseline terms of the k-ω model as well as additional terms needed to account for compressibility effects. At present there is no satisfactory, practically applicable solution to the problem concerning the influence of

turbulence on chemical production terms ($\dot{W}_i$). Probability density function methods and lately, large eddy simulation approaches, introduce additional uncertainties in the form of additional constants. There is also a lack of appropriate experimental data to confirm the degree of their accuracy for hypersonic flows. Consequently, turbulence closure effects on chemical production terms, $\dot{W}_i$, are not considered in the above formulation of the investigated flowfield:

$$\mathbf{S} = \frac{1}{J}\begin{bmatrix} \dot{W}_1 \\ \vdots \\ \dot{W}_{ns} \\ 0 \\ \vdots \\ 0 \\ 0 \\ P_k - \rho k\omega - \rho k\omega f(M_T) \\ \frac{\omega}{k}\left(\frac{5}{9}P_k + \frac{5}{6}\rho k\omega\right) + \rho\omega^2 f(M_T) \end{bmatrix} \tag{4}$$

The dilatational dissipation correction terms [that is the ones involving $f(M_T)$] are necessary to account for the reduced growth of shear layers when the convective Mach number is high [13,14]. The Wilcox [15] dilatational dissipation model specifies $f(M_T) = 3/2\max(0, M_T^2 - 1/16)$. This improves the baseline k-ω equations in solving high convective Mach number shear layers without underpredicting the skin friction in high Mach number boundary layers, at least up to a freestream Mach number of six. More compressible corrections exist [16], but due to very little or no empirical data to justify their presence, their effect is neglected in the present study. From the exact form of the transport equation for k, the turbulent kinetic energy production term can be written in generalized coordinates as

$$P_k = \sum_{i=1}^{nd}\sum_{j=1}^{nd}\left(-\frac{2}{3}\rho k X_{i,j}\frac{\partial v_j}{\partial X_i} + \mu^\star \sum_{m=1}^{nd}\sum_{n=1}^{nd} J\beta_{i,j}^{m,n}\frac{\partial v_n}{\partial X_j}\frac{\partial v_m}{\partial X_i}\right) \tag{5}$$

III. Numerical Method

The discretized governing equations together with the boundary conditions are solved on a generalized structured mesh using the window allocatable resolver for propulsion (WARP) code. A detailed description of the computational technique employed in the WARP code can be found in [7]. All partial derivatives are discretized using second-order accurate, centered finite difference stencils except for the convection derivative, which is discretized using the approximate Riemann solver of Roe [17] and made second-order accurate through a symmetric minmod limiter by Yee et al. [18]. The discretized residual is solved to steady state using a block-implicit factorization algorithm [19] including the analytical Jacobian derived from the chemical model and a linearization strategy of the viscous terms by Chang and Merkle [20]:

$$\prod_{i=1}^{nd}\left[I + \Delta\tau\delta_{X_i}\frac{\partial \mathbf{F}_i}{\partial \mathbf{Q}} - \Delta\tau\delta_{X_i}(\mathbf{K}_{i,i}\delta_{X_i}\mathbf{B}) - \delta_{1,i}\Delta\tau\mathbf{C}^-\right]\Delta\mathbf{Q} = -\Delta\tau\mathbf{R}_\Delta \tag{6}$$

with $\mathbf{B} \equiv \partial\mathbf{G}/\partial\mathbf{Q}$ the linearization Jacobian of the viscous terms and $\mathbf{C}^- \equiv \partial\mathbf{S}^-/\partial\mathbf{Q}$ the linearization Jacobian of the chemical and negative turbulent source terms. Only the negative turbulent source terms are linearized to ensure the stability of the implicit algorithm. The term $\delta_{X_i}\partial\mathbf{F}_i/\partial\mathbf{Q}$ is determined by the linearization of the first-order Roe scheme with the Roe Jacobian locally frozen [21,22]. Although more costly per iteration compared with a lower-upper symmetric Gauss–Seidel inversion strategy, approximate factorization is chosen here for its ability to solve the Roe scheme without the need for introducing an explicit artificial dissipation term in the residual (the entropy correction) to stabilize the iterative process. The introduction of the entropy correction adds additional artificial dissipation to the numerical scheme, which affects the accuracy of the solution considerably [23].

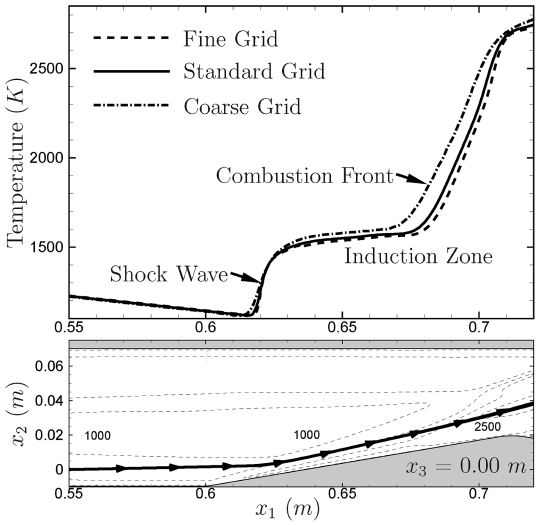

Fig. 1 Grid convergence of temperature along a streamline.

The quantity ξ is defined as the maximum between the sum of the discretized continuity residuals and the energy conservation residual divided by $\mathbf{Q}$:

$$\xi \equiv \max\left(\frac{\sum_{k=1}^{ns}|\mathbf{R}_{\Delta,k}|}{J^{-1}\rho}, \frac{|\mathbf{R}_{\Delta,ns+nd+1}|}{J^{-1}\rho E}\right) \tag{7}$$

For all cases considered, ξ decreases through at least 5 orders of magnitude and convergence is reached when ξ for all nodes falls below $\xi_{\text{converge}} = 400\ \text{s}^{-1}$. The pseudotime step, $\Delta\tau$, is fixed to the geometric average between the minimum and maximum Courant–Friedrichs–Lewy (CFL) conditions, which is found to give faster convergence than the minimum CFL condition for cases involving high mesh aspect ratios.

The WARP code has been validated against the following experimental data obtained for a number of hypervelocity flows similar to those simulated herein: Settles et al. [24] shock wave/turbulent boundary layer interaction at $M = 2.84$, Burrows and Kurkov's [25] wall fuel injection mixing and combusting flowfield, Waitz et al. [26] Mach 6 fuel/air mixing by a ramp injector, Donohue et al. [27] Mach 2 swept ramp injector mixing problem, Mao et al. [28] Mach 3 wall fuel injection at a 15° angle, and Lehr's [29] blunt-body detonation and shock-induced combustion in a Mach 5 stoichiometric H_2/air flow. In all cases considered agreement of the numerical predictions were well within limits acceptable in the hypersonic propulsion research community. For more details on the validation effort and the various levels of agreement see [8,30].

A. Grid Convergence Study

In an effort to assess the grid-induced error in the shcramjet combustor, a similar combustor configuration and nonhomogeneous inflow is solved with a standard grid density of $201 \times 280 \times 105 = 5.9$ million grid cells. The grid density is similar to that used for the combustor results presented, but on a slightly different streamwise domain. The solution was also determined on a coarse grid with half the number of nodes in each dimension (0.7 million) and on a fine grid with double the number of nodes in each dimension (47.2 million). Figure 1 illustrates the temperature variation along a streamline in the $x_3 = 0.0$ m plane originating at $x_1 = 0.55$ and $x_2 = 0.0$ m for each of the three grid densities. The greater the grid density, the farther downstream the shock and detonation wave are initiated. For the streamline shown in Fig. 1, there is a maximum difference in temperature between the coarse and standard grid of 11% (195 K) and between the standard and fine grid of 4% (81 K).

The maximum temperature reached through the detonation wave is within 0.3% (6 K) for all grid densities. Similar trends are found in the rest of the flowfield. Integrated values are influenced by the slight delay in the combustion process on the finer grid densities, with the thrust potential increase occurring slightly downstream. The regular grid density provides a 0.6% greater maximum thrust potential than the fine and coarse grid density cases that have the same value.

B. Boundary Conditions

Only the spanwise segment of the airframe containing the interior engine flow path is examined. The assumption is made that infinite spanwise fuel injector arrays are representative of the fuel/air mixing process away from the side-walls of the engine. Hence, second-order symmetry conditions are imposed on the spanwise sides of the computational domain, which lie along the centerline of adjacent staggered injectors on opposite walls, at $x_3 = 0.00$ and $x_3 = 0.02$ m. The initial x_1 engine inflow plane is specified as supersonic inflow and the end outflow plane as a zeroth order supersonic outflow. Domain boundaries in the x_2 direction are set as zeroth order supersonic outflow. All wall surfaces are assumed to be no-slip, noncatalytic, and cooled to an arbitrarily chosen constant temperature, 500 K for the shock-induced combustion ramjet and 800 K for the scramjet, with quantities at the walls determined by a second-order extrapolation from the interior flow. At the wall $k = 0$, while the specific dissipation rate $\omega = 36\mu/5\rho d_w^2$ as given by Wilcox [10]. To maintain practical grid sizes, node spacing at the wall surfaces is $d_w = 25$ μm up until the end of the fuel injector arrays and $d_w = 10$ μm thereafter. The value of y^+ varies through the domain between 0.406 and 6.604, with the highest values being found in regions with high pressure and temperature.

C. Freestream Conditions

In the Wilcox k-ω model [10], the turbulent kinetic energy is set to a small value in the freestream to prevent division by zero in the dissipation rate source term, Eq. (4). However, in the present study, in the freestream $k = 0$ and $\tilde{k}$ is defined as

$$\tilde{k} = \max\left[k, \min\left(k_{\text{div}}, \frac{\omega\mu}{\rho}\right)\right] \tag{8}$$

with k_{div} a user-specified constant that is generally set lower than one-tenth of the maximum value of k throughout the boundary layer [7]. This is verified numerically not to affect the laminar sublayer, but to improve the robustness and efficiency of the integration significantly. The minimum between k_{div} and $\omega\mu/\rho$ is taken so that a clipping occurs *only* in nonturbulent flow regions in which an accurate representation of ω does not affect the accuracy of the flowfield. A value of k_{div} of 1000 m^2/s^2 is used for all cases and is verified to be below the maximum value of k in the boundary layer, which for the present case is between 40,000 and 70, 000 m^2/s^2. The freestream ω is set to 10 m^{-1} times the freestream velocity as suggested by Wilcox, which is 100–1000 times smaller then the maximum ω value present at all x_1 planes.

IV. Global Performance Parameters

The concept of mixing efficiency quantifies the fuel/air mixing process. The fuel-based mixing efficiency, η_m, at a streamwise plane of interest (denoted by subscript b), is defined as the ratio of the fuel that would burn in the plane to the mass flux of fuel entering the engine:

$$\eta_m = \int_b c^R_{\text{H}_2}\, \text{d}\dot{m}/(\dot{m}_{\text{fuel}}) \tag{9}$$

The mass fraction of reacting fuel, $c^R_{\text{H}_2}$, is given as

$$c^R_{\text{H}_2} = \min(c_{\text{H}_2}, c^S_{\text{H}_2} \cdot c_{\text{O}_2}/c^S_{\text{O}_2}) \tag{10}$$

with the stoichiometric mass fraction of oxygen, $c^S_{\text{O}_2}$, equal to 0.2284 and the stoichiometric mass fraction of hydrogen, $c^S_{\text{H}_2}$, equal to 0.02876. Note that this formulation does not take into account the flammability limits of hydrogen in air, which are $0.1 < \phi < 7.0$ at standard pressure and have been shown to lie above $\phi = 0.8$ for cases similar to the ones studied here [31].

The concept of thrust potential [9,32,33] is used in the present study to evaluate the propulsive effectiveness of the hypersonic engine components when significant total temperature variations are present. The thrust potential determines how much thrust a section of the engine would develop by taking the difference in momentum of stations at the end of the section (outlet) and the tip of the inlet (reference). The outlet momentum is found from a reversible expansion of the flow at the outlet station (subscript b) to an iteratively determined back pressure at the nozzle exit area of the vehicle (subscript c) [33]. All irreversible losses occurring ahead of station b in the propulsive flow path, due to shocks, mixing processes, and friction, are reflected in the numerically determined magnitude of the flow momentum at that station. Thrust potential, $\mathcal{F}_{\text{pot}}$, is thus defined as

$$\mathcal{F}_{\text{pot}} = -\mathcal{F}_{\text{pot,ref}} + \int_b \frac{\rho_c q_c^2 + p_c^*}{\rho_c q_c}\, \text{d}\dot{m}/\dot{m}_{\text{air,engine}} \tag{11}$$

The reference thrust potential is the negative of the oncoming airflow momentum at the initial cross-section of the engine per unit mass of the airflow entering the engine, i.e. $\mathcal{F}_{\text{pot,ref}} = (\rho_0 v_0^2 + p_0)A_0/\dot{m}_{\text{air,engine}} = 3411$ N · s/kg. The thrust potential at the initial engine cross-section is thus zero.

The propulsive characteristics such as overall thrust and specific impulse, as well as the magnitudes of the total frictional forces acting on the entire, finite span, engine from tip to tail, were quantified as follows. The thrust of the vehicles is here determined by the forces acting on their surfaces. The force on the engine walls due to the pressure is taken as the negative of the inviscid momentum terms on the wall surfaces:

$$\mathcal{F}_{\text{pressure},i} = \sum_{\text{surface nodes}} \Delta X_i[-\mathbf{F}_i] \tag{12}$$

where the sum is taken over all surfaces with wall boundary conditions. The term ΔX_i is a directional variable that corresponds to $+1$ or -1 depending whether the normal to the surface is in the positive or negative X_i direction. The skin friction is found as the negative of the viscous momentum on the wall surfaces:

$$\mathcal{F}_{\text{friction},i} = \sum_{\text{surface nodes}} \Delta X_i \left[\sum_{j=1}^{nd} \mathbf{K}_{i,j} \frac{\partial \mathbf{G}}{\partial X_j}\right] \tag{13}$$

where in both Eqs. (12) and (13) only the momentum components of the vectors on the right side are used. The thrust generated by the fuel entering the engine is determined from its momentum:

$$\mathcal{F}_{\text{fuel},i} = -\Delta X_i(\rho v_i^2 + p)_{\text{fuel}} A_{\text{fuel}} \tag{14}$$

where A_{fuel} is the fuel injection cross-sectional area. The total thrust and lift, which are positive in the $-x_1$ and x_2 directions, respectively, are the sum of the pressure, friction, and fuel thrust forces. The specific impulse, I_{sp}, can be used for comparison of the performance of different engines:

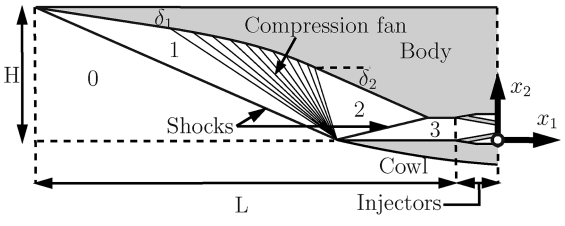

Fig. 2 Mixed-compression inlet configuration.

Table 1 Inlet characteristics

Vehicle	Scramjet	Shcramjet
Length (L), m	6.375	3.834
Height (H), m	1.278	0.484
Compression ratio (P_3/P_0)	172.58	30.98
Area ratio (A_3/A_0)	21.48	8.14
Exit Mach number	3.72	5.58
Exit thrust potential, N · s/kg	−111.90	−70.07

$$I_{sp} = \frac{-(\mathcal{F}_{\text{pressure},1} + \mathcal{F}_{\text{friction},1} + \mathcal{F}_{\text{fuel},1})}{g\dot{m}_{\text{fuel}}} \tag{15}$$

where g is gravitational acceleration.

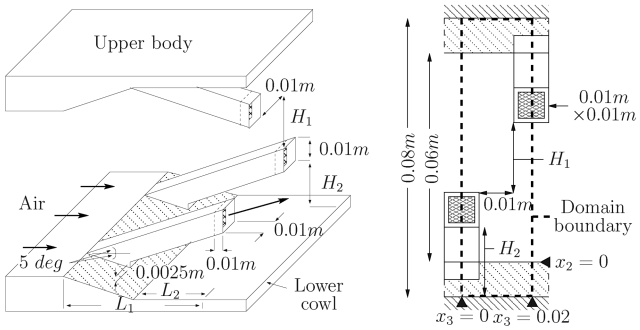

a) Isometric view **b) x_2-x_3 domain**

Fig. 4 Cantilevered ramp injector array geometry.

V. Methodology of Comparative Analysis

Comparison of the aeropropulsive performance characteristics of the two vehicles is performed herein at a flight Mach number of 11, considered to be the lower limit at which the expected advantages of the shock-induced combustion ramjet over the scramjet could be realized. At an altitude of 34.5 km, corresponding to a flight dynamic pressure of 67.03 kPa (1400 psf), the oncoming airflow conditions are: a pressure of 601 Pa, temperature of 235 K and a velocity of 3391 m/s. The comparative analysis is performed by assuming that both ramjets share the same: inlet type, fuel properties and injection systems, mixing and/or combustor geometry and nozzle design methodology. The WARP code is used for both cases with identical gridding technique. For each engine, no attempt has been made to apply specific optimization techniques to improve their respective component efficiencies.

A. Inlet

A generic inlet is employed consisting of: a leading edge shock followed by a Prandtl–Meyer centered compression ramp; a final shock redirecting the inlet exit flow in the flight direction, see Fig. 2. The degree of compression is fixed by specifying the magnitude of the inlet exit flow temperature, T_3, after the final shock. To avoid premature ignition in the fuel/air mixing duct of the shcramjet, the inlet exit temperature or the mixing duct entrance flow temperature must be kept below the auto-ignition temperature of hydrogen. Hence for the shcramjet engine T_3 is fixed at 800 K. The choice of the burner entry flow temperature for the scramjet is limited by material and air dissociation temperature considerations. Its inlet exit flow temperature T_3 is herein set to 1500 K.

The entire two-dimensional inlet flowfield is then numerically simulated in a structured grid using the WARP code subject to the aforementioned initial and boundary conditions. The resulting inlet sizes and magnitudes of flow variables at the exit of the inlet for both vehicles are summarized in Table 1. Axial velocity distributions at the inlet exit, shown in Fig. 3a, exhibit a fairly uniform flow with boundary layer thicknesses of the order of 14.4 and 8.3 mm for the scramjet and 10.0 and 6.7 mm for the shcramjet for the upper and lower duct walls, respectively. The losses incurred by the inlet flow due to shocks and frictional forces on the internal walls are quantified by the concept of thrust potential. Figure 3b depicts their evolution for both engines. Note that the origin of the coordinate system is placed at the exit plane of the fuel injectors and the plane parallel to the inlet upper cowl surface (see Fig. 2).

B. Fuel Injector and Mixing/Combustor Duct

Gaseous hydrogen is injected into the mixing/combustor duct via a system of cantilevered ramp injectors previously investigated in detail for a shock-induced combustion ramjet [9,30], see Fig. 4. They have proved to be particularly suited to keep the combustible mixture away from the boundary layers of the duct walls in shcramjet engines. Although other fuel injection systems could be more appropriate for a scramjet engine, for purposes of the present comparative analysis, they are employed in the scramjet engine as well. The arrays are placed on the upper and lower walls at the entrance of the internal duct of the engine in a staggered manner.

Conditions imposed on the fuel injection properties are: a stagnation temperature below 1700 K, static pressure matched to the surrounding air, and an equivalence ratio of 1.0. A 10 mm long runway is used inside the fuel injectors before the plane of injection to reduce the solutions sensitivity to the freestream value of ω, which is known to cause difficulties in k-ω schemes. Fuel injector geometries, as noted in Fig. 4, and the fuel inflow properties for both

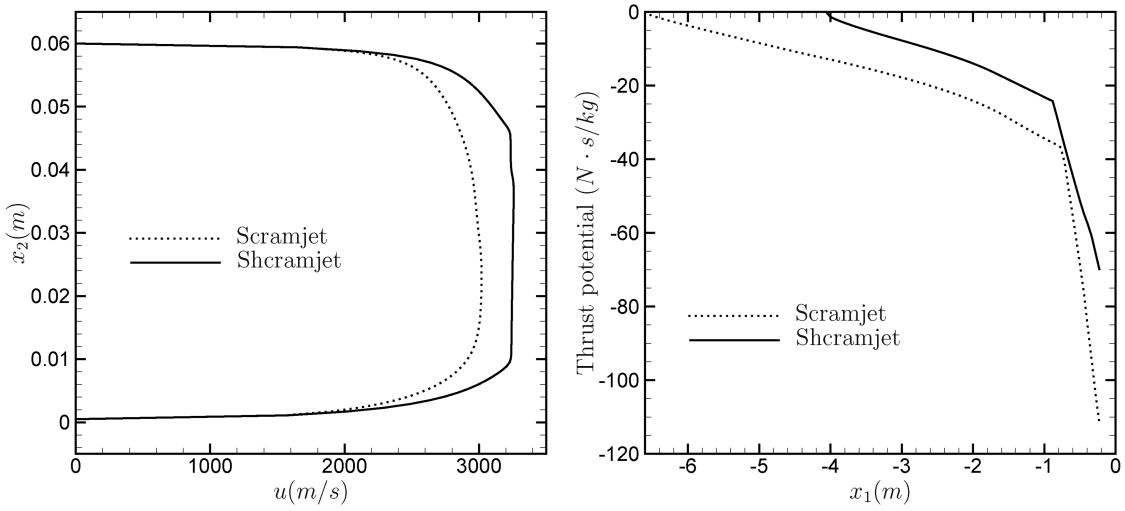

a) Inlet exit velocity profiles **b) Thrust potential losses in the inlet**

Fig. 3 Inlet performance.

Table 2 Fuel injection parameters

Vehicle	Scramjet	Shcramjet
L_1, m	0.169	0.226
L_2, m	0.057	0.111
H_1, m	0.015	0.02
H_2, m	0.03	0.02
Fuel velocity, m/s	5652	6229
Fuel temperature, K	561	309
Fuel pressure, Pa	95,000	18,000
Fuel/air equivalence ratio	1.0	1.0

the scramjet and shock-induced combustion ramjet are given in Table 2. The shock-induced combustion ramjet has longer injectors to deposit the fuel in the center of the air stream and avoid premature ignition caused by fuel entering the hot boundary layers. While similar injectors are used for the scramjet, they are shorter as there is no requirement to avoid ignition. The injectors protrude less into the flow and are positioned in the center of the lower or upper half of the duct to maximize mixing with equal amounts of air above and below the fuel.

The hydrogen mass fraction distributions in the mixing duct of the shock-induced combustion ramjet are shown in Fig. 5 for x_1 planes through the length of the mixing duct. H_2 mass fraction contours extend exponentially from 0.01 to 1.0, with the stoichiometric mass fraction lying at 0.02876. The shock-induced combustion ramjet produces fuel/air mixture in the vertical center of the mixing duct, away from the boundary layers along the walls.

The evolution of the mixing efficiency, η_m, and thrust potential, $\mathcal{F}_{\text{pot}}$, are shown in Fig. 6. The sharp increase in $\mathcal{F}_{\text{pot}}$ at the fuel exit plane, $x_1 = 0$ m, is due to the momentum of the injected hydrogen. Thereafter it gradually decreases due to mixing and frictional losses in the duct. At the exit of the mixing duct, $x_1 = 0.45$ m and $\eta_m = 0.48$.

No flame-holding device is employed in the scramjet combustor. Rather the diffusive burning process of the stoichiometrically injected hydrogen is assumed to take place spontaneously at the thermogas-dynamic conditions prevailing in the vicinity of the fuel injection region. With Jachimowski's [11] chemical kinetics model for H_2/air combustion, the ignition delay is 0.02 m downstream of the injection point, as seen in Fig. 7, where contours of temperature and H_2O mass fractions are presented in the $x_3 = 0.01$ m plane, midway between the spanwise flow symmetry planes. The corresponding variation of the thrust potential in the scramjet combustor is depicted in Fig. 6.

The combustible mixture in the mixing duct of the shcramjet is ignited via a 15 ° wedge formed by a bend in the lower cowl wall at $x_1 = 0.45$ m from the point of fuel injection plane. This is believed to result in an appropriate balance between the thrust potential loss and mixing efficiency gain. Because of the highly nonuniform and inhomogeneous nature of the oncoming combustible mixture, the shock-induced combustion process is highly three-dimensional. Figure 8 shows the Mach number and temperature contours in the $x_3 = 0.01$ m plane of the shock-induced combustion process. Mach numbers, normal to the shock-induced combustion wave, are also shown and indicate the complex shock-induced-detonation wave nature of the resulting combustion process. The corresponding rise in the thrust potential is given in Fig. 6.

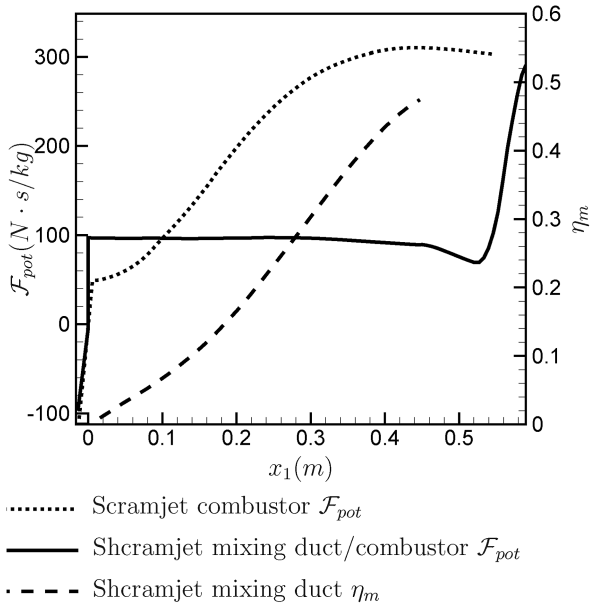

Fig. 6 Thrust potential and mixing efficiency in the mixing duct/combustor.

C. Nozzle

For each type of hypersonic vehicle, the nozzle wall contours are designed via the method of characteristics (MOC). From the flow properties at the spanwise center of the computational plane, the two-dimensional MOC for rotational flows is used to construct the upper and lower contours of the nozzle in the plane. For the MOC, the flow is assumed to be chemically frozen and inviscid. The MOC is subject to the following conditions: the exhaust gases are directed parallel to the flight direction to recover maximum thrust, and the exit pressure is determined (iteratively) to terminate the nozzle upper wall at the height of the inlet tip, in order to avoid unnecessary drag. To account for the development of the turbulent boundary layers on the nozzle walls, Edenfield's [34] experimental correlations are used to determine the displacement thickness, which is then used to adjust the MOC obtained contours by a vertical distance, such that the viscous flow matches the inviscid contour mass flow rate.

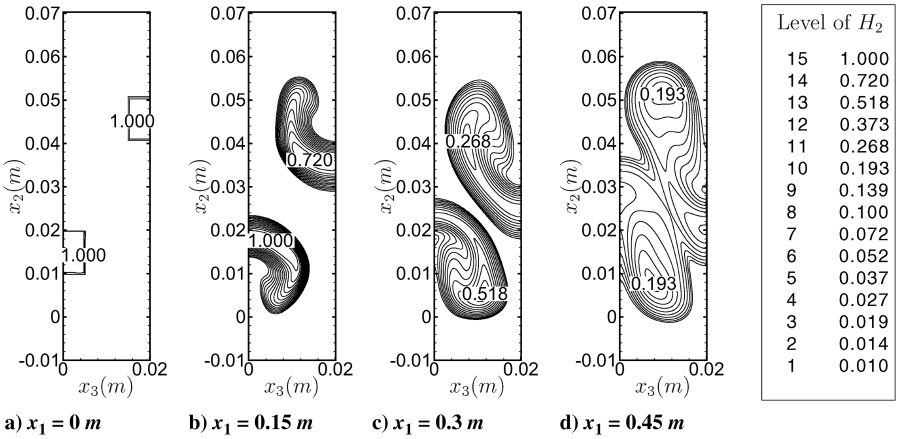

a) $x_1 = 0$ *m* **b) $x_1 = 0.15$ *m*** **c) $x_1 = 0.3$ *m*** **d) $x_1 = 0.45$ *m***

Fig. 5 Hydrogen mass fraction contours in the mixing duct of the shcramjet.

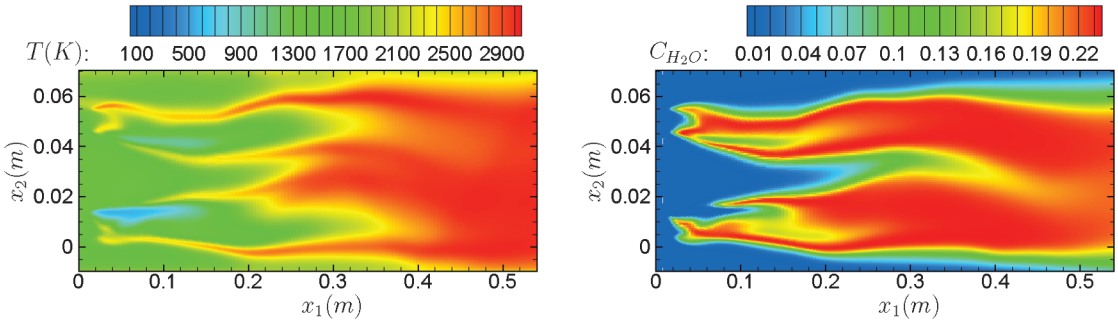

a) Temperature **b) H_2O mass fraction**

Fig. 7 Contour plots at $x_3 = 0.01$ m in the scramjet combustor.

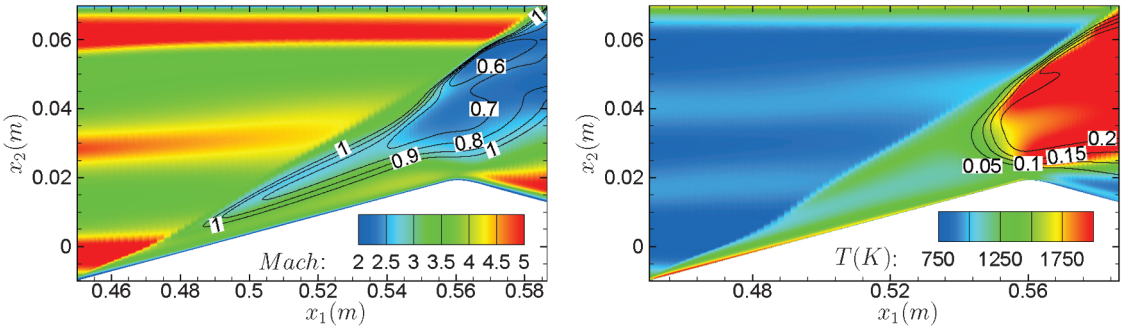

a) Absolute mach number field with overlaid normal mach contours **b) Temperature field with overlaid C_{H_2O} contours**

Fig. 8 Contour plots at $x_3 = 0.01$ m in the shcramjet combustor.

The streamwise location for the start of the scramjet nozzle is chosen as the location where the thrust potential reaches a maximum, indicating the momentum addition from the combustion process is being overwhelmed by the friction in the duct, Fig. 6. For the scramjet, the false-wall technique [35] is used, which assumes the flow along the cowl internal surface is equivalent to a streamline at the center of a complete nozzle. For the shock-induced combustion ramjet, the dual wall technique [36,37] is used to determine the nozzle wall contours due to the combustor exit's upward flow component. The initial starting line for the nozzle expansion on the body surface is the location where the combustion-inducing shock impinges the body wall, Fig. 9. Expanding the flow at this location mitigates the size of the resulting shock-induced combustion wave/boundary layer interaction generated recirculation zone on the body surface. Prior studies have shown that expansion at this location does not adversely affect the engine performance [38]. On the cowl, the expansion on the wedge occurs 0.11 m downstream from the start of the wedge. This distance is sufficient to ensure the combustion was not quenched by the flow expansion.

Since the resulting nozzle wall contours generated from the MOC are exceedingly long, they are truncated to provide 87 and 98% of the maximum thrust generated by the lower cowl and upper body wall, respectively, in the shcramjet (resulting only in a small gain of 20 s in the fuel-specific impulse as compared with equal truncation of both walls) and 95% of the upper and lower walls in the scramjet, to reduce frictional drag, outer cowl pressure drag and weight. This results in a nozzle that is 64% the length of the original MOC generated contour for the shcramjet and 46% for the scramjet. The nozzle and cowl wall contours thus generated in the spanwise center computational plane are assumed to prevail over the entire lateral span of the three-dimensional computational domain. The nozzle walls contours are blended smoothly into the existing combustor walls with four-degree polynomials. The outer surface of the cowl was contoured by a third-degree polynomial passing through the cowl leading and trailing edges, forming at these points inclusion angles of 5 deg. Subsequent to determining the nozzle wall contours, the entire three-dimensional reacting vehicle flowfields, including the nozzles, are numerically simulated using the WARP code. The employed numerical grid is shown in Fig. 10. The pressure contours in the spanwise center domain, $x_3 = 0.01$ m, are shown in Figs. 11 and 12. Because of significant pressure differences between the inner flow and the flow outside the cowl, a shock is formed at the trailing edge of the cowl.

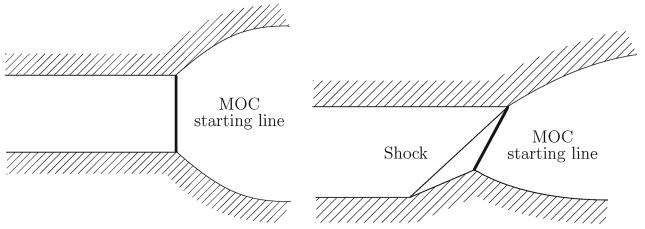

a) Scramjet nozzle **b) Shcramjet nozzle**

Fig. 9 Starting line of the nozzle expansion process.

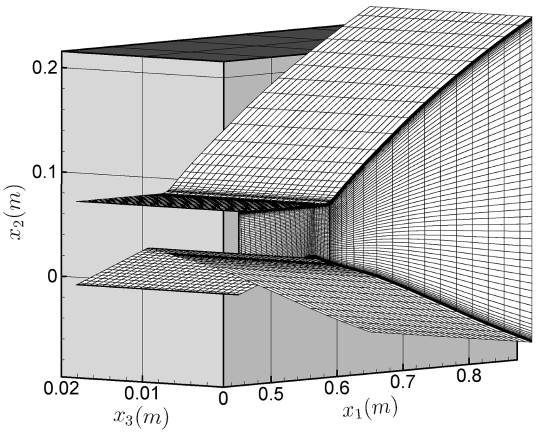

Fig. 10 Every fourth grid line of the shcramjet nozzle domain.

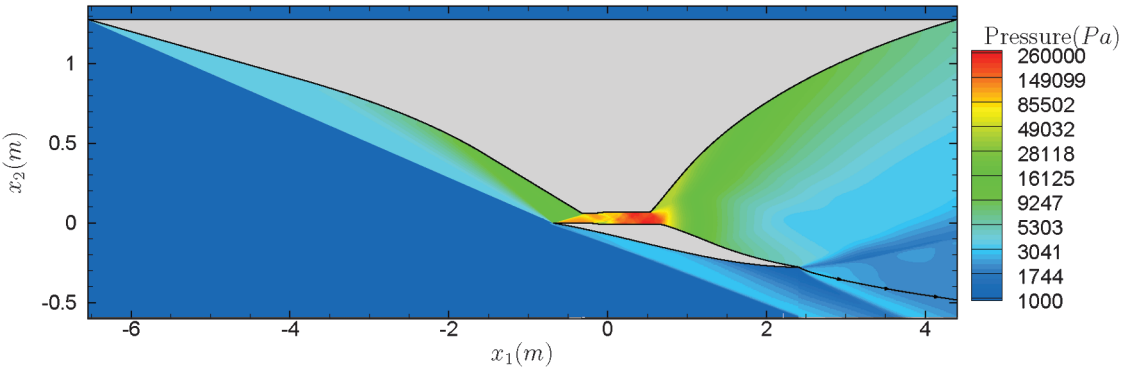

Fig. 11 Scramjet pressure contours at $x_3 = 0.01$ m.

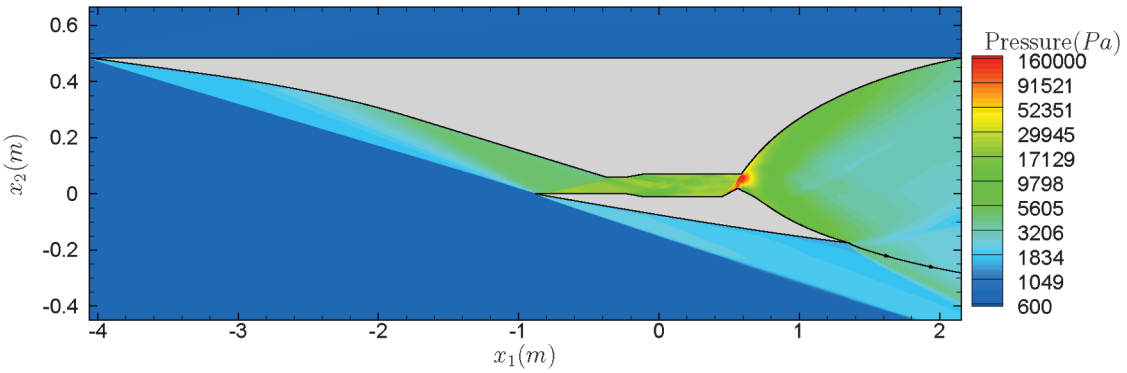

Fig. 12 Shcramjet pressure contours at $x_3 = 0.01$ m.

The mass flow through the interior of the engines reside above the shear layer originating from the end of the cowl, represented by the streamlines in Figs. 11 and 12. For the shock-induced combustion ramjet, this flow covers a height of 0.77 m by the end of the engine, which is 58% larger than the inlet airflow capture height. In the scramjet the flow through the interior of the engine covers a height of 1.77 m at the end of the nozzle, 38% larger than the inlet airflow capture height.

For the shock-induced combustion ramjet, the Mach number at the nozzle exit is approximately 4.42 and the average nozzle exit velocity is 3498 m/s. Since the nozzle was truncated in length, the exit plane flow is not parallel to the x_1 axis, but expands outwards with angles ranging from −5.3 to 5.7 deg. In the scramjet, the exit Mach number is approximately 4.35, the average nozzle exit velocity is 3503 m/s, and the flow expands outwards with angles ranging from −4.4 to 8.3 deg.

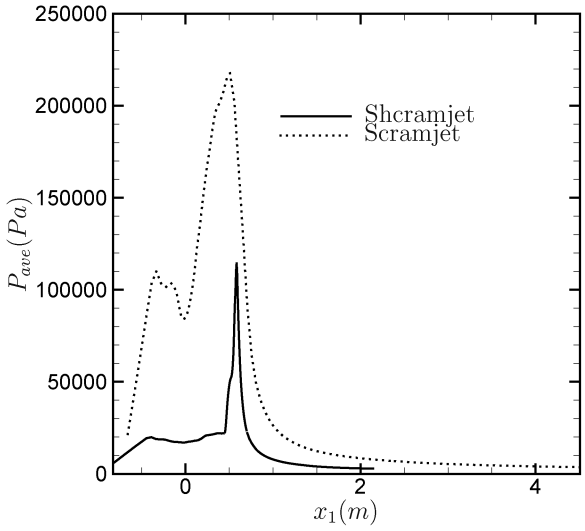

Fig. 13 Mass-averaged pressure variations along the engine.

VI. Comparative Engine Performance

Simulations of the flows in the engine components outlined above allow the performance characteristics of the entire vehicle to be analyzed. The total grid for the entire vehicle consist of 27.6 and 29.5 million nodes for the shcramjet and scramjet, respectively.

The level of pressures reached in both engine cycles is shown in Fig. 13, where the pressure variations, mass-flux-averaged over x_1 planes, are depicted from the inlet cowl tip to the end of the nozzle. It can be seen that the maximum pressure level reached in the scramjet is higher than that of the shcramjet. The variations of the cumulative pressure and frictional forces acting in the x_1-direction (the direction opposite to flight) on the internal walls of the engine (wetted by the propulsive flowpath) in both vehicles are presented in Figs. 14 and 15. Note that the upstream face of the combustion-inducing wedge in the shcramjet produces the largest amount per length of friction and pressure drag in the engine, 64.6% of the pressure drag and 11% of the friction drag, which is 43.1% of the total drag while only being 1.8% of the length of the engine. The effectiveness of such an engine is thus strongly dependent upon having a shock-generating device that assures combustion with minimal drag losses. The scramjet produces greater friction over its larger engine surfaces. Its combustor accounts for 46.0% of the total frictional drag. Figure 16 shows the evolution of the fuel-specific impulse along the entire length of both vehicles. The fuel-specific impulse is determined from the thrust generated by integrating pressure and frictional forces on all four wetted surfaces of the vehicle and from fuel injection. It can be seen that the shcramjet and the scramjet provide a fuel-specific impulse of 1109 and 1450 s, respectively.

The relative sizes of the resulting vehicles are summarized in Table 3. The shcramjet is appreciably smaller and thus lighter than the scramjet with a length of 6.2 m and height of 0.66 m compared

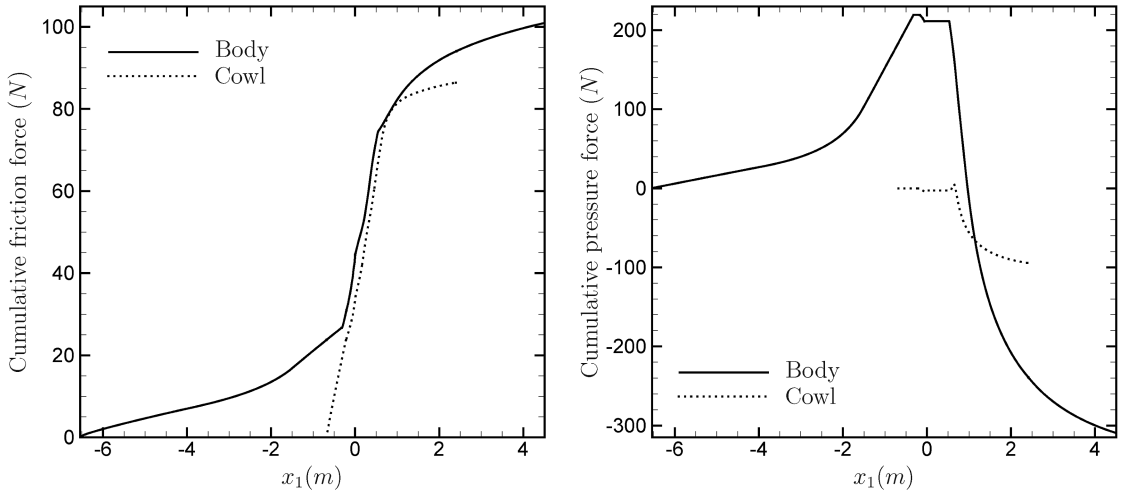

a) x_1 friction forces **b) x_1 pressures forces**

Fig. 14 Forces on scramjet inner wall surfaces.

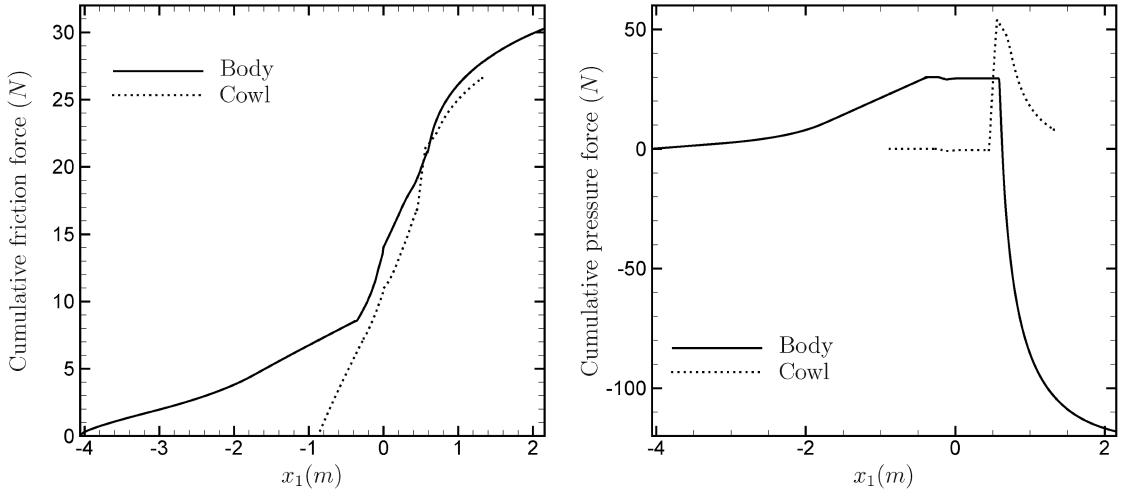

a) x_1 friction forces **b) x_1 pressures forces**

Fig. 15 Forces on shcramjet inner wall surfaces.

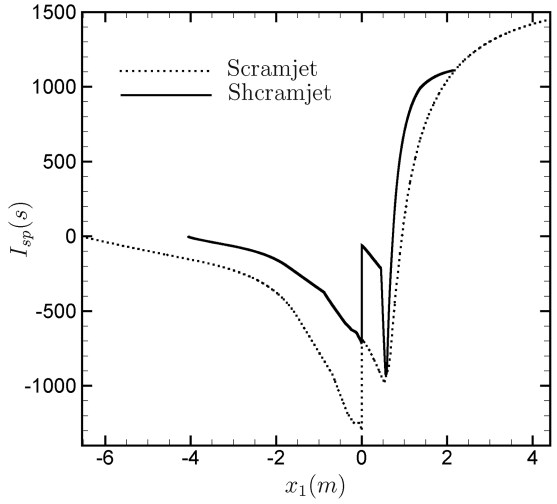

Fig. 16 Variations of the fuel-specific impulse along the vehicles.

with 10.95 and 1.56 m, respectively, for the scramjet. Note that the combustor lengths of the shcramjet and scramjet are 0.11 and 0.54 m, respectively. Table 3 summarizes the aeropropulsive performance characteristics of both engines.

Table 3 Overall vehicle performance characteristics

Vehicle	Scramjet	Shcramjet
Length, m	10.95	6.2
Height, m	1.56	0.66
Span, m	0.02	0.02
$\dot{m}_{\text{air}}$, kg/s	0.771	0.299
$\dot{m}_{\text{fuel}}$, kg/s	0.02321	0.008797
Combustor length, m	0.54	0.11
$\mathcal{F}_{\text{friction}}$, N	198.7	64.38
$\mathcal{F}_{\text{pressure}}$, N	−389.91	−103.61
I_{sp}, s	1450	1109

VII. Conclusions

The performed numerical comparative analysis of the aeropropulsive characteristics of a scramjet and a shcramjet revealed that at the considered flight conditions of $M_0 = 11$, the scramjet still outperforms the shcramjet with a fuel-specific impulse of 1450 s as compared with the 1109 s developed by the shcramjet. However, the shcramjet is appreciably smaller with a length about two-thirds of that of the scramjet. Its combustor length is approximately one-fifth of that of the scramjet requiring less cooling by excess fuel. Therefore, it is much lighter than a scramjet. It is believed that an ongoing similar comparative analysis at a flight Mach number of 16

will clearly delineate the interval of flight Mach numbers where the shock-induced combustion ramjet outperforms the scramjet in all its aeropropulsive characteristics.

References

[1] Morrison, R. B., "Evaluation of the Oblique Detonation Wave Ramjet," NASA CR 145358, 1978.

[2] Morrison, R. B., "Oblique Detonation Wave Ramjet," NASA CR 159192, 1980.

[3] Ostrander, M. J., Hyde, J. C., Young, M. F., and Kissinger, R. D., "Standing Oblique Detonation Wave Engine Performance," AIAA Paper 87-2002, 1987.

[4] Menees, G. P., Adelman, H. G., Cambier, J. L., and Bowles, J. V., "Wave Combustor for Trans-Atmospheric Vehicles," *Journal of Propulsion and Power*, Vol. 8, No. 3, 1992, pp. 709–713. doi:10.2514/3.23536

[5] Dudebout, R., Sislian, J. P., and Oppitz, R., "Numerical Simulation of Hypersonic Shock-Induced Combustion Ramjets," *Journal of Propulsion and Power*, Vol. 14, No. 6, 1998, pp. 869–879. doi:10.2514/2.5368

[6] Heiser, W. H., and Pratt, D. T., *Hypersonic Airbreathing Propulsion*, AIAA Education Series, AIAA, Washington, D. C., 1994.

[7] Parent, B., and Sislian, J. P., "The Use of Domain Decomposition in Accelerating the Convergence of Quasihyperbolic Systems," *Journal of Computational Physics*, Vol. 179, No. 1, 2002, pp. 140–169. doi:10.1006/jcph.2002.7048

[8] Parent, B., and Sislian, J. P., "Validation of Wilcox k-ω Model for Flows Characteristic to Hypersonic Airbreathing Propulsion," *AIAA Journal*, Vol. 42, No. 2, 2004, pp. 261–270. doi:10.2514/1.1989

[9] Alexander, D. C., and Sislian, J. P., "A Computational Study of the Propulsive Characteristics of a Shcramjet Engine," *Journal of Propulsion and Power*, Vol. 24, No. 1, 2008, pp. 34–44. doi:10.2514/1.29951

[10] Wilcox, D. C., "Reassessment of the Scale Determining Equation for Advanced Turbulence Models," *AIAA Journal*, Vol. 26, No. 11, 1988, pp. 1299–1310. doi:10.2514/3.10041

[11] Jachimowski, C. J., "An Analytical Study of Hydrogen–Air Reaction Mechanism with Application to Scramjet Combustion," NASA TP 2791, 1988.

[12] McBride, B. J., and Reno, M. A., "Coefficients for Calculating Thermodynamic and Transport Properties of Individual Species," NASA TM 4513, 1993.

[13] Dimotakis, P. E., *Turbulent Free Shear Layer Mixing and Combustion*, AIAA, Washington, DC, 1991, pp. 265–340.

[14] Papamoschou, D., and Roshko, A., "Compressible Turbulent Shear Layer: An Experimental Study," *Journal of Fluid Mechanics*, Vol. 197, Dec. 1988, pp. 453–477. doi:10.1017/S0022112088003325

[15] Wilcox, D. C., "Dilatation-Dissipation Corrections for Advanced Turbulence Models," *AIAA Journal*, Vol. 30, No. 11, 1992, pp. 2639–2646. doi:10.2514/3.11279

[16] Coakley, T. J., Horstman, C. C., Marvin, J. G., Viegas, J. R., Bardina, J. E., Huang, P. G., and Kussoy, M. I., "Turbulent Compressibility Corrections," NASA TM 108827, May 1994.

[17] Roe, P. L., "Approximate Riemann Solvers, Parameter Vectors, and Difference Schemes," *Journal of Computational Physics*, Vol. 43, No. 2, 1981, pp. 357–372. doi:10.1016/0021-9991(81)90128-5

[18] Yee, H. C., Klopfer, G. H., and Montagné, J. L., "High-Resolution Shock-Capturing Schemes for Inviscid and Viscous Hypersonic Flows," *Journal of Computational Physics*, Vol. 88, No. 1, 1990, pp. 31–61. doi:10.1016/0021-9991(90)90241-R

[19] Beam, R. M., and Warming, R. F., "An Implicit Factored Scheme for the Compressible Navier–Stokes Equations," *AIAA Journal*, Vol. 16, No. 4, 1978, pp. 393–402. doi:10.2514/3.60901

[20] Chang, C. L., and Merkle, C. L., "The Relation Between Flux Vector Splitting and Parabolized Schemes," *Journal of Computational Physics*, Vol. 80, No. 2, 1989, pp. 344–361. doi:10.1016/0021-9991(89)90104-6

[21] Coakley, T. J., and Huang, P. G., "Turbulent Modelling for High-Speed Flows," AIAA Paper 92-04366, 1992.

[22] Batten, P., Leschziner, M. A., and Goldberg, U. C., "Average-State Jacobians and Implicit Methods for Compressible Viscous and Turbulent Flows," *Journal of Computational Physics*, Vol. 137, No. 1, 1997, pp. 38–78. doi:10.1006/jcph.1997.5793

[23] Parent, B., Sislian, J. P., and Schumacher, J., "Numerical Investigation of the Turbulent Mixing Performance of a Cantilevered Ramp Injector," *AIAA Journal*, Vol. 40, No. 8, 2002, pp. 1559–1566. doi:10.2514/2.1824

[24] Settles, G. S., Vas, I. E., and Bogdonoff, S. M., "Details of a Shock-Separated Turbulent Boundary Layer at a Compression Corner," *AIAA Journal*, Vol. 14, No. 12, 1976, pp. 1709–1715. doi:10.2514/3.61513

[25] Burrows, M. C., and Kurkov, A. P., "Analytical and Experimental Study of Supersonic Combustion of Hydrogen in a Vitiated Air Stream," NASA TMX 2828, 1973.

[26] Waitz, I. A., Marble, F. E., and Zukoski, E. E., "Investigation of a Contoured Wall Injector for Hypervelocity Mixing Augmentation," *AIAA Journal*, Vol. 31, No. 6, 1993, pp. 1014–1021. doi:10.2514/3.11723

[27] Donohue, J. M., McDaniel, J. C., and Haj-Hariri, H., "Experimental and Numerical Study of Swept Ramp Injection into a Supersonic Flowfield," *AIAA Journal*, Vol. 32, No. 9, 1994, pp. 1860–1867. doi:10.2514/3.12184

[28] Mao, M., Riggins, D. W., and McClinton, C. R., "Numerical Simulation of Transverse Fuel Injection," NASA N91–21062 13–02, Lewis Research Center, 1991.

[29] Lehr, H. F., "Experiments in Shock-Induced Combustion," *Astronautica Acta*, Vol. 17, Nos. 4–5, 1972, pp. 589–597.

[30] Alexander, D. C., Sislian, J. P., and Parent, B., "Hypervelocity Fuel/Air Mixing in Mixed-Compression Inlets of Shcramjets," *AIAA Journal*, Vol. 44, No. 10, 2006, pp. 2145–2155. doi:10.2514/1.12630

[31] Schwartzentruber, T. E., Sislian, J. P., and Parent, B., "Suppression of Premature Ignition in the Premixed Inlet Flow of a Shcramjet," *Journal of Propulsion and Power*, Vol. 21, No. 1, 2005, pp. 87–94. doi:10.2514/1.7003

[32] Riggins, D. W., McClinton, C. R., and Vitt, P. H., "Thrust Losses in Hypersonic Engines Part 1: Methodology," *Journal of Propulsion and Power*, Vol. 13, No. 2, 1997, pp. 281–289. doi:10.2514/2.5160

[33] Parent, B., and Sislian, J. P., "Effect of Geometrical Parameters on the Mixing Performance of Cantilevered Ramp Injectors," *AIAA Journal*, Vol. 41, No. 3, 2003, pp. 448–456. doi:10.2514/2.1966

[34] Edenfield, E. E., "Design of a High Reynolds Number Mach Number 8 Contoured Nozzle for the Hypervelocity Wind Tunnel," Arnold Engineering Development Center, AEDC-TR 72-48, Aug. 1972.

[35] Park, H.-K., "Model of an Aero-space Plane Based on an Idealized Cone-derived Waverider Forebody," Ph.D. Thesis, Univ. of Oklahoma, Norman, OK, 1990.

[36] Migal, D., "Supersonic Annular Nozzles," *Journal of Spacecraft and Rockets*, Vol. 9, No. 1, 1972, pp. 3–6. doi:10.2514/3.61623

[37] Veen, R. V., Gentry, R., and Hoffman, J. D., "Design of Shrouded-Plug Nozzles for Maximum Thrust," *AIAA Journal*, Vol. 12, No. 9, 1974, pp. 1193–1197. doi:10.2514/3.49452

[38] Alexander, D. C., "Hypersonic Mixed-Compression Inlet Shock-Induced Combustion Ramjets," Ph.D. Thesis, Graduate Department of Aerospace Science and Engineering, Univ. of Toronto, Toronto, ON, Canada, 2006.

J. Powers
Associate Editor